membranes

MDPI

Article

Comparison of Sb_2O_3 and Sb_2O_3/SiO_2 Double Stacked pH Sensing Membrane Applied in Electrolyte-Insulator-Semiconductor Structure

Chyuan-Haur Kao [1,2,3,4], Kuan-Lin Chen [1], Hui-Ru Wu [5], Yu-Chin Cheng [5], Cheng-Shan Chen [5], Shih-Ming Chen [5], Ming-Ling Lee [6,*] and Hsiang Chen [5,*]

1 Department of Electronic Engineering, Chang Gung University, 259 Wen-Hwa 1st Road, Kwei-Shan, Taoyuan 333, Taiwan; chkao@mail.cgu.edu.tw (C.-H.K.); chkao@mail.cgu.edu (K.-L.C.)
2 Kidney Research Center, Department of Nephrology, Chang Gung Memorial Hospital, Chang Gung University, No.5, Fuxing St., Guishan, Taoyuan 333, Taiwan
3 Department of Electronic Engineering, Ming Chi University of Technology, 284 Gungjuan Rd., Taishan Dist., New Taipei City 24301, Taiwan
4 Center for Green Technology, Chang Gung University, 259 Wen-Hwa 1st Road, Kwei-Shan, Taoyuan 333, Taiwan
5 Department of Applied Materials and Optoelectronic Engineering, National Chi Nan University, Puli 545, Taiwan; s109328037@mail1.ncnu.edu.tw (H.-R.W.); s109328027@mail1.ncnu.edu.tw (Y.-C.C.); s107328012@mail1.ncnu.edu.tw (C.-S.C.); s107328009@mail1.ncnu.edu.tw (S.-M.C.)
6 Department of Electro-Optical Engineering, Minghsin University of Science and Technology, No.1, Xinxing Rd., Xinfeng, Hsinchu 304, Taiwan
* Correspondence: mingling@must.edu.tw (M.-L.L.); hchen@ncnu.edu.tw (H.C.)

check for updates

Citation: Kao, C.-H.; Chen, K.-L.; Wu, H.-R.; Cheng, Y.-C.; Chen, C.-S.; Chen, S.-M.; Lee, M.-L.; Chen, H. Comparison of Sb_2O_3 and Sb_2O_3/SiO_2 Double Stacked pH Sensing Membrane Applied in Electrolyte-Insulator-Semiconductor Structure. *Membranes* **2022**, *12*, 734. https://doi.org/10.3390/membranes12080734

Academic Editor: Konstantin Mikhelson

Received: 14 April 2022
Accepted: 22 July 2022
Published: 26 July 2022

Abstract: In this study, electrolyte-insulator-semiconductor (EIS) capacitors with Sb_2O_3/SiO_2 double stacked sensing membranes were fabricated with pH sensing capability. The results indicate that Sb_2O_3/SiO_2 double stacked membranes with appropriate annealing had better material quality and sensing performance than Sb_2O_3 membranes did. To investigate the influence of double stack and annealing, multiple material characterizations and sensing measurements on membranes including of X-ray diffraction (XRD), X-ray photoelectron spectroscopy (XPS), and scanning electron microscopy (SEM) were conducted. These analyses indicate that double stack could enhance crystallization and grainization, which reinforced the surface sites on the membrane. Therefore, the sensing capability could be enhanced, Sb_2O_3/SiO_2-based with appropriate annealing show promises for future industrial ion sensing devices.

Keywords: Sb_2O_3/SiO_2 double stack; pH sensing; silicate; crystallization; reiability

1. Introduction

In the 1980s, an enzyme sensor based on an electrolytic insulator semiconductor [1,2] (EIS) capacitive structure was demonstrated, which had a very simple structure. These EIS sensors consist of a dielectric layer [3] and are deposited on a silicon substrate [4]. The EIS sensor is immersed in a sample solution to form a capacitance structure and the capacitance of the structure changes [5] depending on the pH value of the contact liquid [6]. As the pH value changes, the flat band capacitance [7] of the EIS chip moves along the voltage axis [8]. Through the change of capacitance [9], the corresponding voltage change [10] can be measured according to the pH value (voltage-capacitance method). In recent years, several kinds of high-k dielectrics [11] have been proposed as sensing membranes such as WO_3 [12], Y_2O_3 [13], Pr_2O3 [14], and HfO_2 [15] to substitute SiO_2 [16] as a sensing membrane due to its low cost, compatibly with silicon, and compact size [17]. However, the dangling bonds and traps in high-k materials may cause great trouble in the future, and these peak applications in sensing devices [18]. SiO_2 as the sensing membrane

still has some advantages such as better crystallization and lower defect density [19]. Therefore, it is possible to have dual advantages by combing SiO_2 and other dielectrics. In this work, double layer Sb_2O_3/SiO_2 [20] sensing films were fabricated. Post-RTA in different temperatures (400 °C, 500 °C, 600 °C) was applied in EIS structure [21]. The sensor performance including sensitivity [22], hysteresis [23], and drift, rate [24], were measured to find the optimal annealing condition [25]. To examine the improvements of material properties, X-ray diffraction (XRD), X-ray photoelectron spectroscopy (XPS), and atomic force microscope (AFM) [26,27] were used to examine the crystalline structure, chemical bindings, and surface roughness. The results indicate that double stack and annealing could enhance crystallization and suppress silicate-related defects [28,29].

2. Experimental

The EIS structures were fabricated on 4-in n-type (100) Si wafers, which have a resistivity of 5–10 Ω-cm. The standard Radio Corporation of America (RCA) cleaning process was performed on the chips. The chip was first immersed in ethanol for 5 min and soaked in DI water for 5 min. Followed by immersion in acetone for 5 min, cleansed in DI water for 5 min, and then isopropyl alcohol was used to remove the organic contaminates. Then, the samples were dipped into 1% hydrofluoric acid to remove native oxide from the surface. A SiO_2 film of 50 nm in thickness was grown on the wafer by dry thermal oxidation. Then, a 50-nm Sb_2O_3 was deposited by radio frequency (RF) reactive sputtering on an n-type silicon wafer and a SiO_2 deposited wafer, respectively. During the RF sputtering, the Sb_2O_3 target was used in the ambient of Ar: O_2 at 20:5. The RF power and pressure were 100 Watt and 20mTorr, respectively. Next, the samples were annealed at different temperatures (400 °C, 500 °C, and 600 °C) by rapid thermal annealing (RTA) in O_2 ambient for 30 s. The back-side contact of the Si wafer was deposited by Al film with 300 nm-thick. Then, the sensing area was defined by a standard photolithography process using a photosensitive epoxy, SU8-2005 of Micro-Chem Inc. (Adel, GA, USA). Finally, the samples were fabricated on the copper lines of the printed circuit board (PCB) by silver gel. As for the sensing dielectric dimensions, the SiO^2 film of 50 nm in thickness was grown on the wafer by thermal dry oxidation. Then, a 50-nm Sb_2O_3 was deposited by radio frequency (rf) reactive sputtering on the SiO_2 film. The sensing area is 0.01 cm^2. The oxide thicknesses were determined by high-frequency (100 kHz) capacitance-voltage (C-V) measurements. The expected error range of the oxide thicknesses for values is about 5–10%. An epoxy package was used to separate the EIS structure and the copper line. The detailed Sb_2O_3/SiO_2 EIS structure is illustrated in Figure 1.

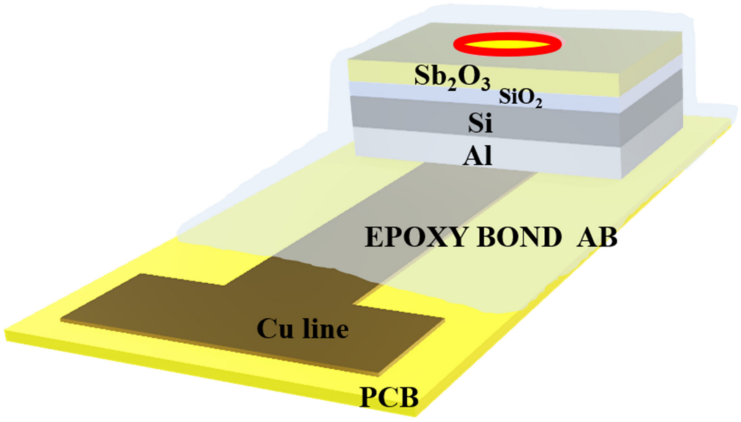

(**a**)

Figure 1. *Cont.*

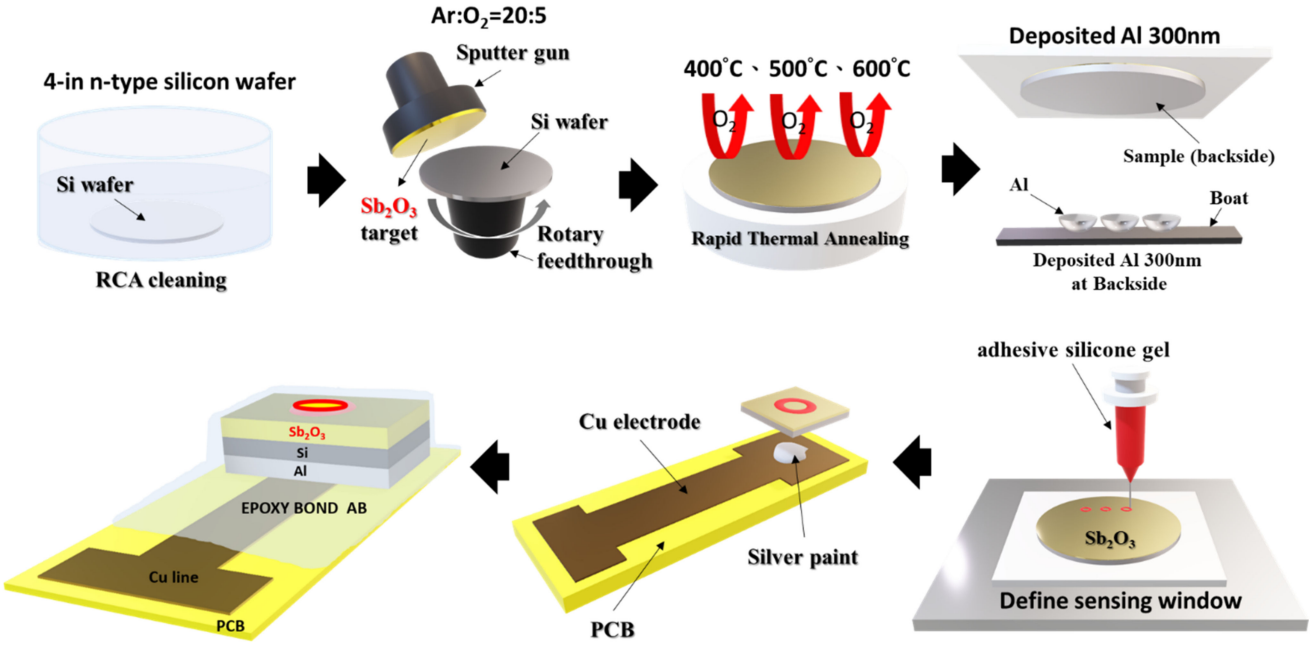

(**b**)

Figure 1. (**a**) The Sb_2O_3/SiO_2 EIS structure. (**b**) The Sb_2O_3 sensing membrane applied to the EIS structure with RTA in O_2 ambient.

Figure 2a,b show the XRD patterns of the Sb_2O_3 layer and Sb_2O_3/SiO_2 layer with various rapid thermal annealing conditions in O_2 treatment. Obviously, in Figure 2a,b three diffraction peaks (222), (400) and (440) can be observed at 27.67°, 32.08°, and 45.96° can be observed for the two types of samples, respectively. When the temperature increased to 500 °C, the peak (222), (400) and (440) intensity increased. Due to enhancement of the crystalline structure during annealing, the peak intensity increased. The two types of samples annealed at a temperature of 500 °C exhibited the strongest peak of (222) and (440) among all of the samples. Moreover, compared with the single-layer (Sb_2O_3), the double-layer structure had a narrow full width at half maximum (FWHM), indicating the grain was larger. In addition, the peaks of the double stacked samples were stronger indicative of strong crystallization. The results reveal that the double-layer (Sb_2O_3/SiO_2) had better crystallization and lower defect density.

To investigate the chemical-binding states in the Sb_2O_3/SiO_2 and Sb_2O_3 sensing membranes, XPS was used. The O 1s spectra for the as-deposited Sb_2O_3 and Sb_2O_3 annealed films are shown in Figure 3a with their appropriate three-peak curve-fitting lines. In the three sets of spectra, the O 1s signal comprised three peaks at 532.9, 531.2 and 530.6 eV, which are SiO_2, Sb-silicate, and Sb_2O_3 respectively. Compared to the single-layer (Sb_2O_3), the intensity of the double-layer (Sb_2O_3/SiO_2) film had a stronger Sb_2O_3 peak and weaker silicate peak, especially for the sample annealed at 500 °C. This was due to the fact that the SiO_2 layer can block Sb atoms from diffusion into the silicon to form silicate. After post-RTA annealing treatment at 500 °C in O_2, the O 1s peak corresponding to Sb–silicate became weaker for the two types of samples indicative of improvement of crystallization and low defect density.

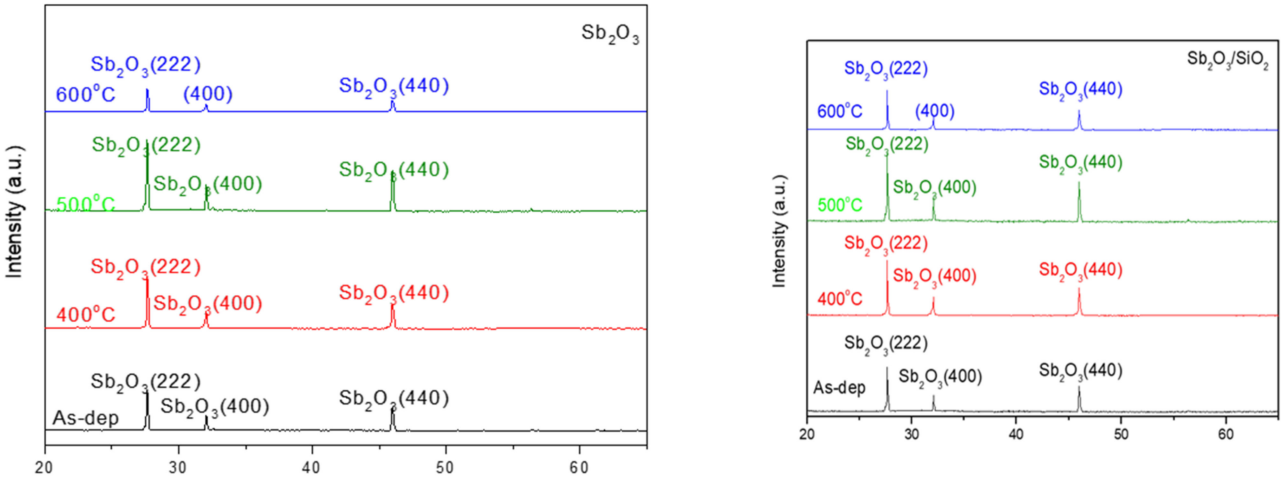

(**a**) (**b**)

Figure 2. XRD patterns of the (**a**) Sb_2O_3 and (**b**) Sb_2O_3/SiO_2 films annealed at various temperatures in O_2 ambient for 30 s.

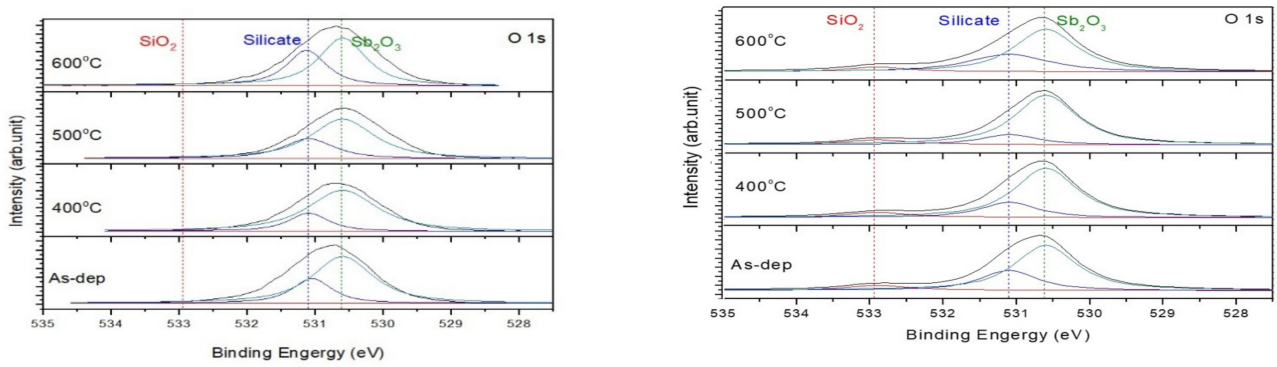

(**a**) (**b**)

Figure 3. The O 1s XPS results of (**a**) Sb_2O_3 film, (**b**) Sb_2O_3/SiO_2 films annealed at various temperatures in O_2 ambient for 30 s.

Furthermore, AFM was used to analyze the surface roughness. shown in Figure 4. The root means square (RMS) values of the Sb_2O_3 films and for the as-dep sample and the samples with RTA annealing from 400 °C to 600 °C were 0.250 nm, 0.267 nm, 0.292 nm, and 0.216 nm while the root means square (RMS) values of the Sb_2O_3/SiO_2 for the as-dep sample and the samples with RTA annealing from 400 °C to 600 °C were 0.261 nm, 0.276 nm, 0.311 nm, and 0.242 nm. AFM was used to analyze the grainization effect of films. Consistent with XRD analysis, the double-layer structure has a narrower full width at half maximum, larger grains can make the surface roughness higher. In the case of 500 °C, there was the optimal lattice structure. As the annealing temperature approached the melting point, the crystal grains gradually disappear and the roughness began to decrease. When the temperature reached 600 °C, the roughness value decreased. This may be due to the fact there were many defects in the film and the lattice structure was destroyed.

To calculate the sensitivity and linearity of the Sb_2O_3 and Sb_2O_3/SiO_2, C-V curves of the samples with various annealing conditions were graphed. The sensitivity values of the as-dep Sb_2O_3 film and the Sb_2O_3 films annealed at 400 °C, 500 °C and 600 °C were 42.25 mV/pH, 45.24 mV/pH, 51.96 mV/pH, and 34.44 mV/pH, respectively. The linearly values of the above four samples were 96.26%, 99.24%, 98.10%, and 82.69%, respectively. The sensitivity values of the as-dep Sb_2O_3/SiO_2, film and the Sb_2O_3/SiO_2, films annealed at 400 °C, 500 °C and 600 °C were 49.42 mV/pH, 49.77 mV/pH, 54.01 mV/pH, and

38.80 mV/pH, respectively. The linearly values of the above four samples were 99.41%, 98.89%, 99.03%, and 95.42%, respectively.

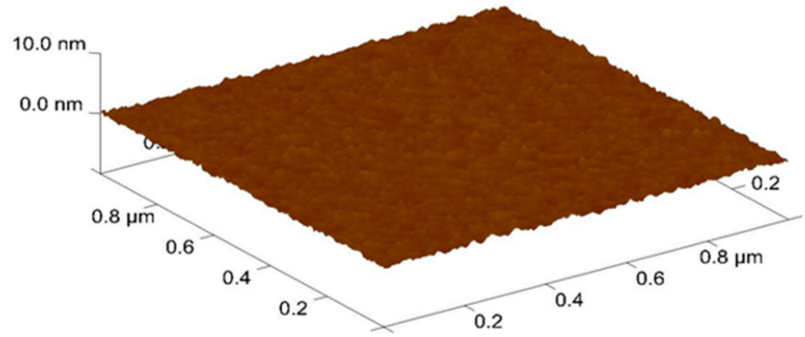

(**a**)

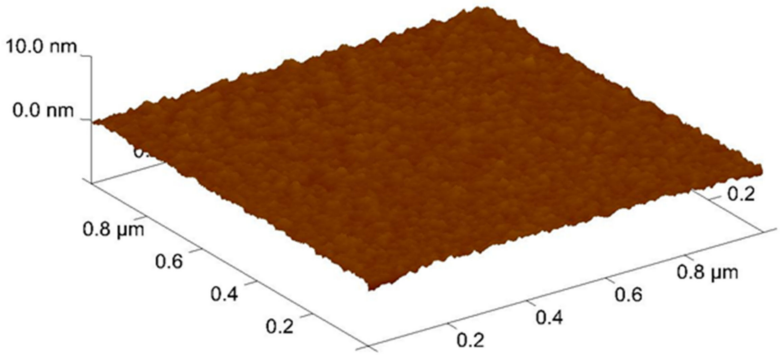

(**b**)

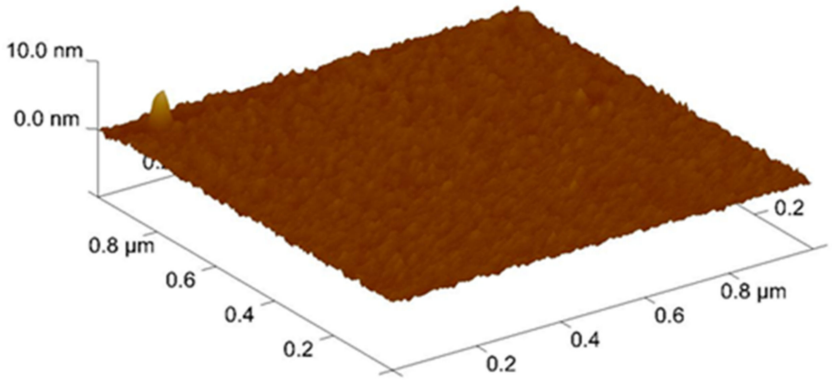

(**c**)

Figure 4. *Cont.*

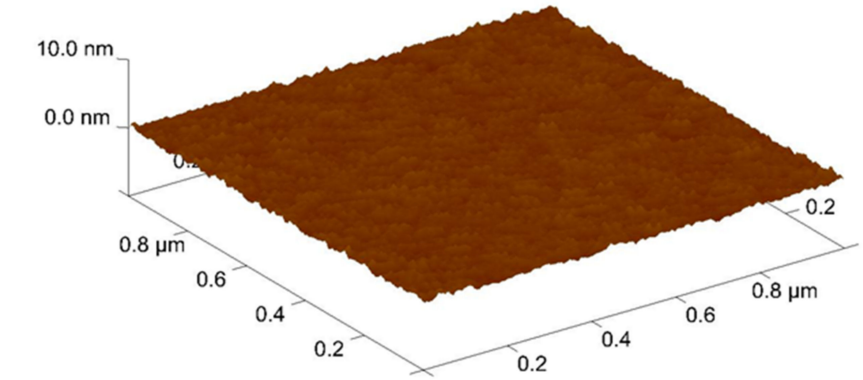

(**d**)

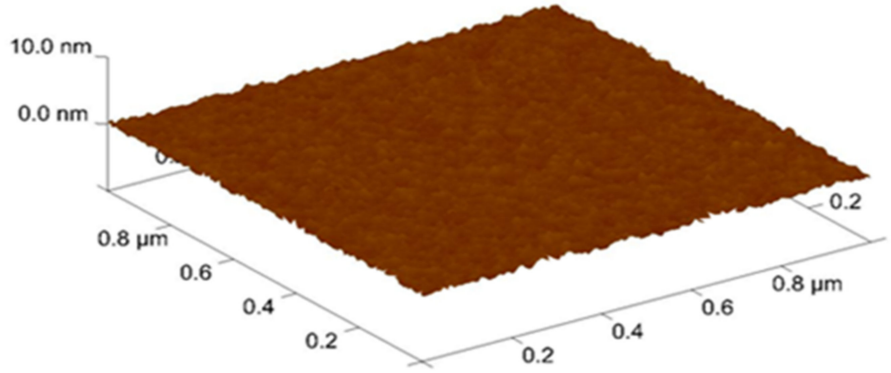

(**e**)

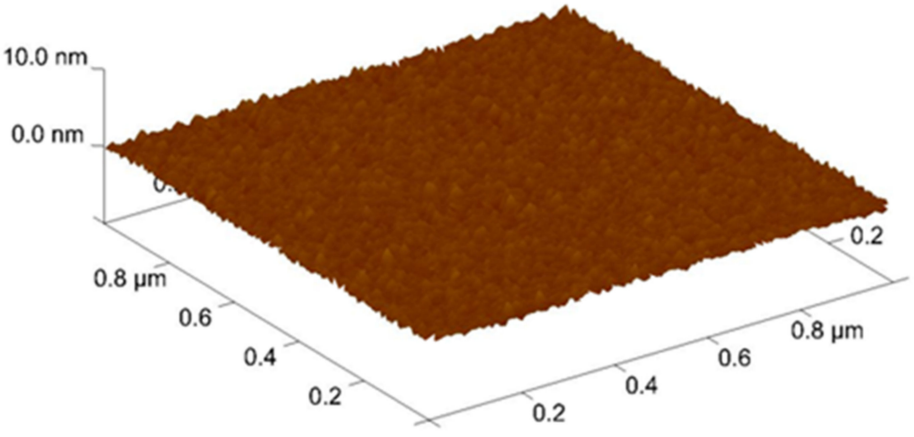

(**f**)

Figure 4. *Cont*.

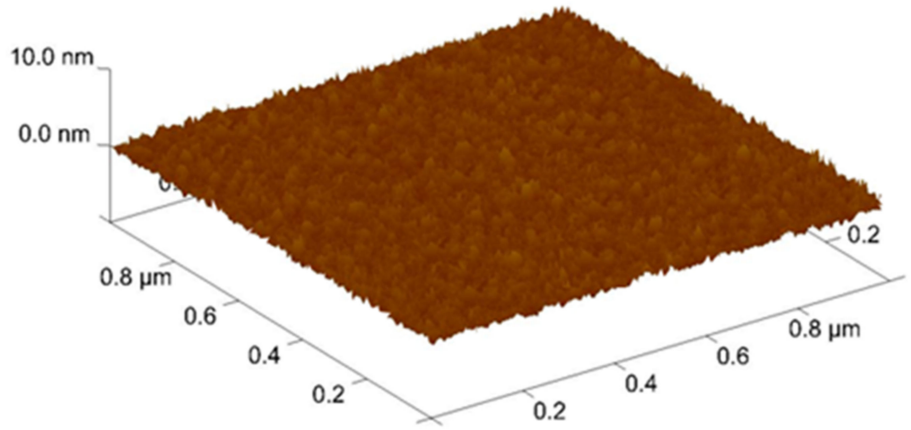

(**g**)

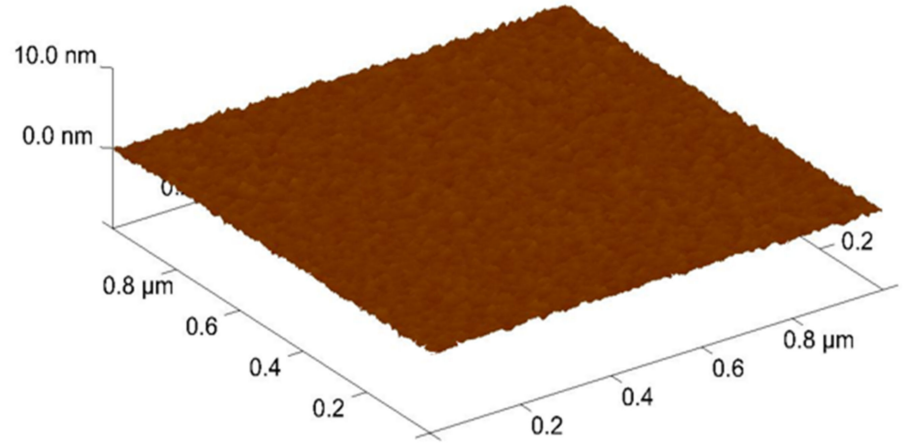

(**h**)

Figure 4. AFM images of Sb_2O_3 film film (**a**) As-dep (**b**) 400 °C (**c**) 500 °C (**d**) 600 °C surface after RF sputter in Ar:O_2 = 20:5 annealing at various temperatures in O_2 ambient for 30 s. AFM images of Sb_2O_3/SiO_2 film (**e**) As-dep (**f**) 400 °C (**g**) 500 °C (**h**) 600 °C surface after RF sputter in Ar:O_2 = 20:5 annealing at various temperatures in O_2 ambient for 30 s.

Figure 5a–d show the C-V curves of the as-dep Sb_2O_3 film, the Sb_2O_3 films annealed at 500 °C the as-dep Sb_2O_3/SiO_2, film and the Sb_2O_3/SiO_2, film annealed at 500 °C. Consistent with material characterizations, the Sb_2O_3/SiO_2 sample annealed in the temperature of 500 °C possessed the highest sensitivity since the annealing at an appropriate temperature could compensate oxygen vacancies to improve the sensing capability. Moreover, with the

addition of the SiO_2 layer, the trapping charges or dangling bonds could be reduced since the thermal grown SiO_2 layer was near-perfect dielectric with fewer defects.

To investigate the hysteresis effects of the membrane, the tested samples were immersed in buffer solutions with different pH values in an alternate cycle (pH 7, pH 4, pH 7, pH 10, and pH 7). The submerging time was five minutes for each solution. We subjected the above samples to a pH loop of 7→4→7→10→7 over 30 min. The hysteresis voltage was defined as the gate voltage difference between the initial and the terminal voltages measured in the above pH loop. The interior sites of defects could react with the ions existing in the tested solution and thus generate hysteresis response.

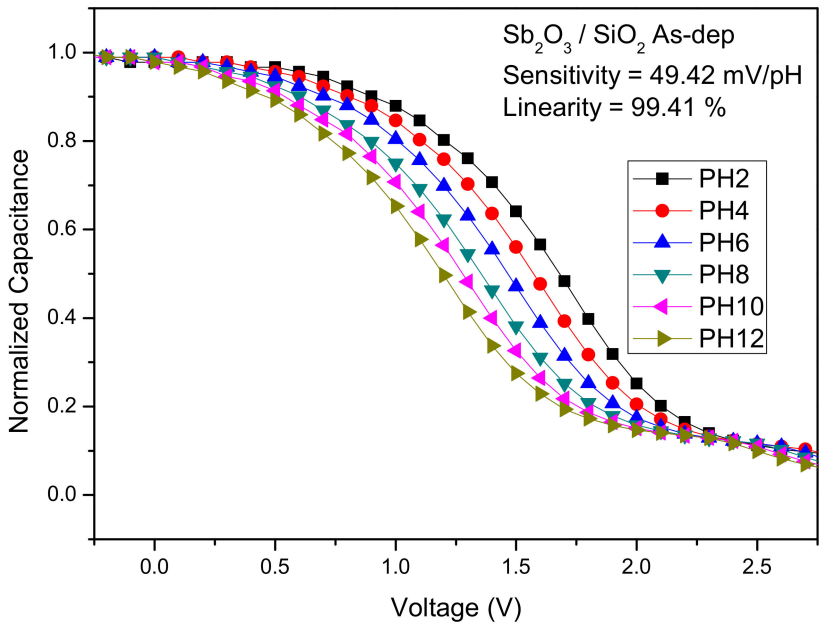

(**a**)

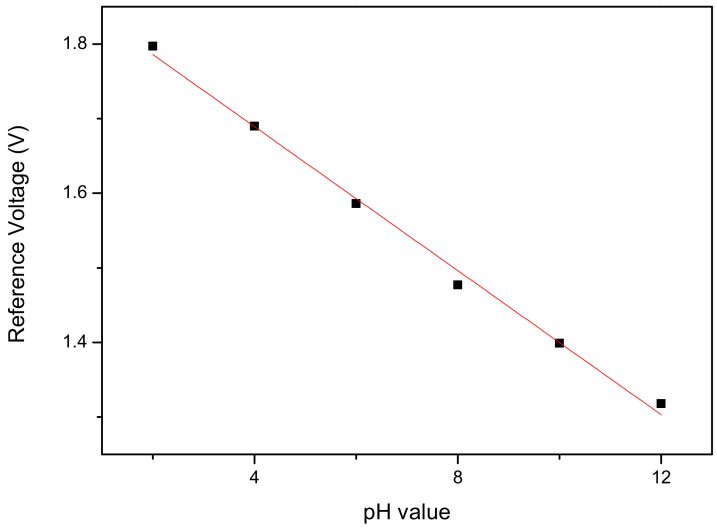

(**b**)

Figure 5. *Cont.*

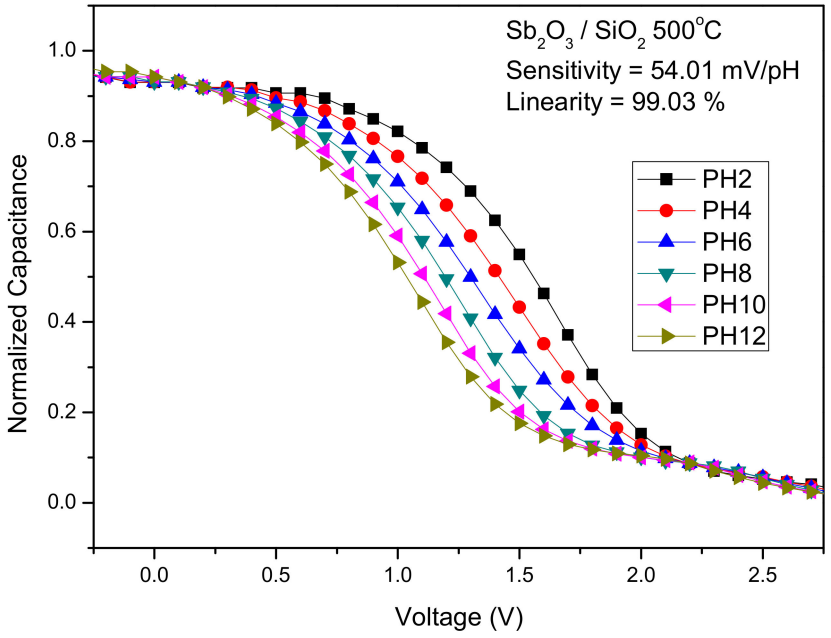

(**c**)

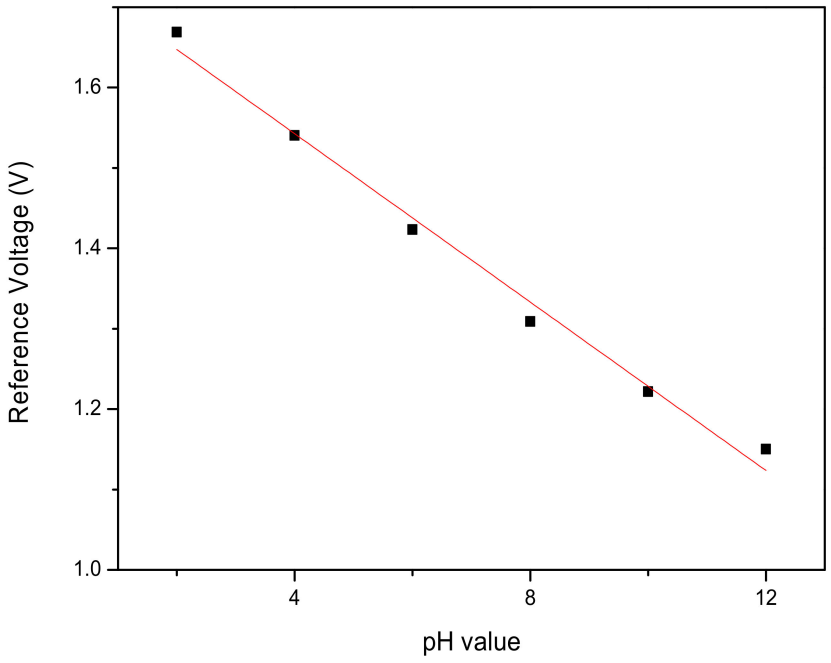

(**d**)

Figure 5. The C-V curves and the extracted sensing data of (**a**) the as-dep Sb_2O_3 film, (**b**) the Sb_2O_3 films annealed at 500 °C, (**c**) the as-dep Sb_2O_3/SiO_2, and (**d**) the Sb_2O_3/SiO_2, film annealed at 500 °C.

Figure 6a shows the hysteresis voltage of the Sb_2O_3 for the as-dep sample and the sample annealed at temperatures from 400 °C, 500 °C, and 600 °C were 47.61 mV, 25.58 mV, 13.82 mV, and 61.98 mV, respectively. Figure 6b shows the hysteresis voltage of the Sb_2O_3/SiO_2 samples for the as-dep sample and the sample annealed at temperatures from 400 °C, 500 °C, and 600 °C were 31.91 mV, 24.42 mV, 12.35 mV, and 36.12 mV, respectively. The Sb_2O_3/SiO_2 sample annealed at a temperature of 500 °C had the lowest hysteresis deviation. The SiO_2 layer could reduce charge loss and increase the reliability of

the interface. Annealing in O_2 ambient could repair the dangling bonding connection and fill the traps in the film.

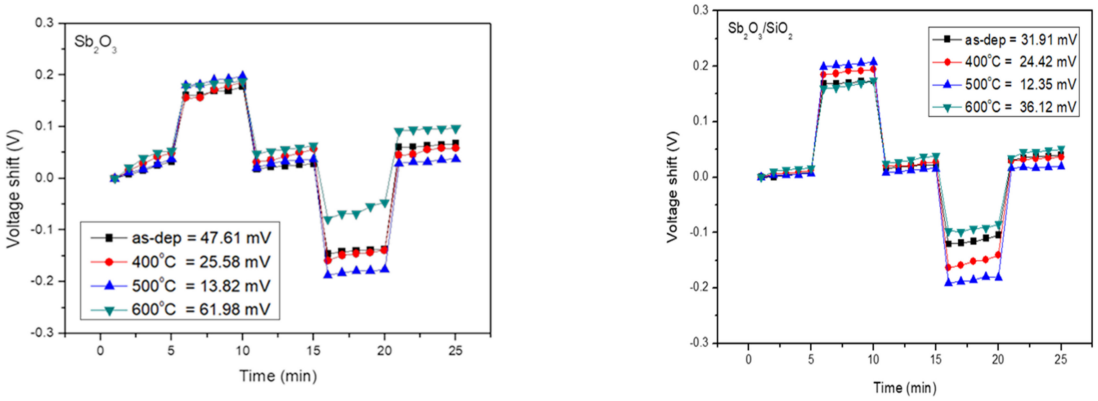

(**a**) (**b**)

Figure 6. (**a**) Hysteresis of Sb_2O_3 sensing membrane with various RTA temperatures in O_2 ambient during the pH loop of 7→4→7→10→7over a period of 30 min. (**b**) Hysteresis of Sb_2O_3/SiO_2 sensing membrane with various RTA temperatures in O_2 ambient during the pH loop of 7→4→7→10→7over 30 min.

To investigate the drift rate of the membrane for long-time reliability, the tested samples were immersed in pH7 buffer solutions and the submerging time was twelve hours. We can use the model of gate voltage drift of pH-ISFET to describe a hopping and/or trap-limited transport mechanism. 'Drift coefficient' is a parameter that describes the long-term stability of a pH sensor. The curves of drift effect of the Sb_2O_3 and Sb_2O_3/SiO_2 sensing film were measured in pH 7 buffer solution for 12 h as shown in Figure 7a,b respectively. Figure 6a shows the drift rate values of the as-dep Sb_2O_3 sample and the Sb_2O_3 samples annealed at 400 °C, 500 °C, and 600 °C were 35.43 mV/h, 8.11 mV/h, 7.25 mV/h, and 12.71 mV/h, respectively. Figure 6b shows the drift rate of the as-dep Sb_2O_3/SiO_2 sample and the Sb_2O_3/SiO_2 samples annealed at 400 °C, 500 °C and 600 °C were 12.56 mV/h, 7.15 mV/h, 6.48 mV/h, and 10.31 mV/h, respectively. The Sb_2O_3/SiO_2 sample annealed in O_2 treatment at a temperature of 500 °C had the lowest hysteresis deviation.

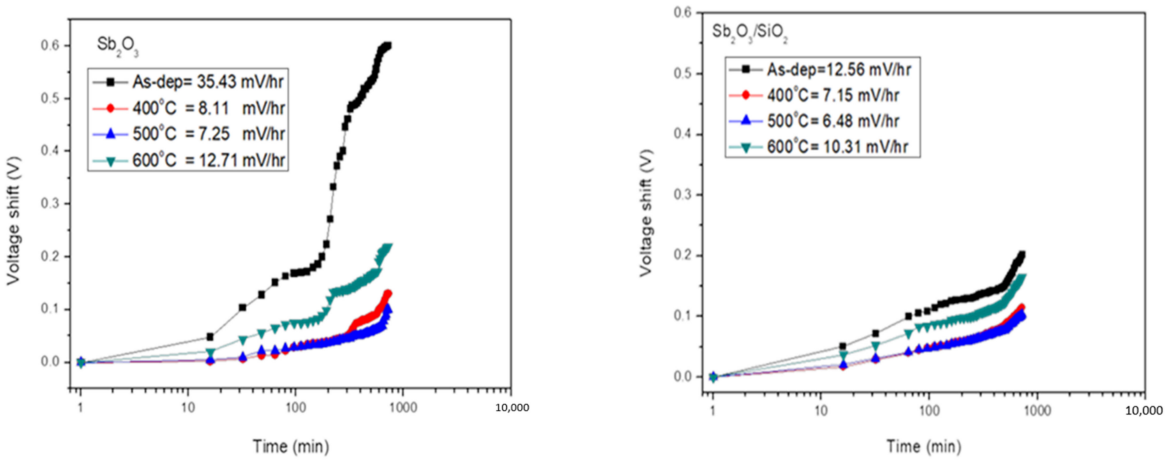

(**a**) (**b**)

Figure 7. (**a**) Drift voltage of Sb_2O_3 sensing membrane annealed with various RTA temperatures in O_2 ambient, then dipped in pH 7 buffer solution for 12 h. (**b**) Drift voltage of Sb_2O_3/SiO_2 sensing membrane annealed with various RTA temperatures in O_2 ambient, then dipped in pH 7 buffer solution for 12 h.

3. Conclusions

In this study, double stacked Sb_2O_3/SiO_2 membranes in EIS structures were fabricated. The double stacked membrane annealed at 500 °C had a higher sensitivity, higher linearity, lower hysteresis voltage, and lower drift rate. Multiple material characterizations indicate that double stack structures and annealing could enhance the crystallization and reduce the defects. Sb_2O_3/SiO_2-based with appropriate annealing show promises for future biomedical sensing devices.

Author Contributions: Conceptualization, C.-H.K., M.-L.L. and H.C.; methodology, C.-H.K. and H.C.; data curation, K.-L.C.; writing—original draft preparation, H.-R.W., Y.-C.C., C.-S.C. and S.-M.C. and H.C.; writing—review and editing, H.C.; visualization, H.C.; supervision, C.-H.K. and H.C.; project administration, H.C.; funding acquisition, M.-L.L. and H.C. All authors have read and agreed to the published version of the manuscript.

Funding: This research was funded by the Ministry of Science and Technology (MOST), Taiwan, grant number "110-2221-E-260-006-" and "110-2222-E-159-002-MY2". The APC was funded by Minghsin University of Science and Technology.

Data Availability Statement: Not applicable.

Acknowledgments: This work was supported by the Ministry of Science and Technology, Taiwan, under the contract of MOST 107-2221-E-260-015-MY3 and "110-2222-E-159-002-MY2".

Conflicts of Interest: There are no conflicts of interest to declare. The funders had no role in the design of the study; in the collection, analyses, or interpretation of data; in the writing of the manuscript; or in the decision to publish the results.

References

1. Song, Z.; Fan, G.-C.; Li, Z.; Gao, F.; Luo, X. Universal design of selectivity-enhanced photoelectrochemical enzyme sensor: Integrating photoanode with biocathode. *Anal. Chem.* **2018**, *90*, 10681–10687. [CrossRef] [PubMed]
2. Streeck, H.; Schulte, B.; Kümmerer, B.M.; Richter, E.; Höller, T.; Fuhrmann, C.; Bartok, E.; Dolscheid-Pommerich, R.; Berger, M.; Wessendorf, L. Infection fatality rate of SARS-CoV2 in a super-spreading event in Germany. *Nat. Commun.* **2020**, *11*, 5829. [CrossRef] [PubMed]
3. Hattori, Y.; Taniguchi, T.; Watanabe, K.; Nagashio, K. Layer-by-layer dielectric breakdown of hexagonal boron nitride. *ACS Nano* **2015**, *9*, 916–921. [CrossRef]
4. Zhang, B.; Liu, Y. A review of GaN-based optoelectronic devices on silicon substrate. *Chin. Sci. Bull.* **2014**, *59*, 1251–1275. [CrossRef]
5. Prakash, S.; Kalaignan, G.P. Investigation of morphological changes on nickel manganese oxide and their capacitance activity. *Colloids Surf. A Physicochem. Eng. Asp.* **2021**, *611*, 125875. [CrossRef]
6. Nie, J.; Ren, Z.; Xu, L.; Lin, S.; Zhan, F.; Chen, X.; Wang, Z.L. Probing contact-electrification-induced electron and ion transfers at a liquid–solid interface. *Adv. Mater.* **2020**, *32*, 1905696. [CrossRef]
7. Hankin, A.; Bedoya-Lora, F.E.; Alexander, J.C.; Regoutz, A.; Kelsall, G.H. Flat band potential determination: Avoiding the pitfalls. *J. Mater. Chem. A* **2019**, *7*, 26162–26176. [CrossRef]
8. Ko, B.-S.; Lee, G.-Y.; Choi, K.-Y.; Kim, R.-Y. A coordinated droop control method using a virtual voltage axis for power management and voltage restoration of dc microgrids. *IEEE Trans. Ind. Electron.* **2018**, *66*, 9076–9085. [CrossRef]
9. Lee, S.-M.; Han, N.; Lee, R.; Choi, I.-H.; Park, Y.-B.; Shin, J.-S.; Yoo, K.-H. Real-time monitoring of 3D cell culture using a 3D capacitance biosensor. *Biosens. Bioelectron.* **2016**, *77*, 56–61. [CrossRef] [PubMed]
10. Chen, K.-H.; Wood, K.N.; Kazyak, E.; LePage, W.S.; Davis, A.L.; Sanchez, A.J.; Dasgupta, N.P. Dead lithium: Mass transport effects on voltage, capacity, and failure of lithium metal anodes. *J. Mater. Chem. A* **2017**, *5*, 11671–11681. [CrossRef]
11. Huang, Y.; Guo, Z.; Liu, H.; Zhang, S.; Wang, P.; Lu, J.; Tong, Y. Heterojunction architecture of N-doped WO_3 nanobundles with Ce_2S_3 nanodots hybridized on a carbon textile enables a highly efficient flexible photocatalyst. *Adv. Funct. Mater.* **2019**, *29*, 1903490. [CrossRef]
12. Italiano, C.; Llorca, J.; Pino, L.; Ferraro, M.; Antonucci, V.; Vita, A. CO and CO_2 methanation over Ni catalysts supported on CeO_2, Al_2O_3 and Y_2O_3 oxides. *Appl. Catal. B Environ.* **2020**, *264*, 118494. [CrossRef]
13. Siakavelas, G.I.; Charisiou, N.D.; AlKhoori, S.; AlKhoori, A.A.; Sebastian, V.; Hinder, S.J.; Baker, M.A.; Yentekakis, I.; Polychronopoulou, K.; Goula, M.A. Highly selective and stable nickel catalysts supported on ceria promoted with Sm_2O_3, Pr_2O_3 and MgO for the CO_2 methanation reaction. *Appl. Catal. B Environ.* **2021**, *282*, 119562. [CrossRef]
14. Tian, X.; Shibayama, S.; Nishimura, T.; Yajima, T.; Migita, S.; Toriumi, A. Evolution of ferroelectric HfO_2 in ultrathin region down to 3 nm. *Appl. Phys. Lett.* **2018**, *112*, 102902. [CrossRef]

15. Pacchioni, G.; Skuja, L.; Griscom, D.L. *Defects in SiO_2 and Related Dielectrics: Science and Technology*; Springer Science & Business Media: Berlin/Heidelberg, Germany, 2012; Volume 2.
16. Spinelle, L.; Gerboles, M.; Kok, G.; Persijn, S.; Sauerwald, T. Review of portable and low-cost sensors for the ambient air monitoring of benzene and other volatile organic compounds. *Sensors* **2017**, *17*, 1520. [CrossRef] [PubMed]
17. Xing, P.; Ma, D.; Ooi, K.J.; Choi, J.W.; Agarwal, A.M.; Tan, D. CMOS-compatible PECVD silicon carbide platform for linear and nonlinear optics. *ACS Photonics* **2019**, *6*, 1162–1167. [CrossRef]
18. Jiang, X.; Ma, Z.; Xu, J.; Chen, K.; Xu, L.; Li, W.; Huang, X.; Feng, D. a-SiN x: H-based ultra-low power resistive random access memory with tunable Si dangling bond conduction paths. *Sci. Rep.* **2015**, *5*, 15762. [CrossRef]
19. Xie, L.-Q.; Chen, L.; Nan, Z.-A.; Lin, H.-X.; Wang, T.; Zhan, D.-P.; Yan, J.-W.; Mao, B.-W.; Tian, Z.-Q. Understanding the cubic phase stabilization and crystallization kinetics in mixed cations and halides perovskite single crystals. *J. Am. Chem. Soc.* **2017**, *139*, 3320–3323. [CrossRef]
20. Abass, K.H.; Obaid, N.H. 0.006 wt.% Ag-Doped Sb_2O_3 Nanofilms with Various Thickness: Morphological and optical properties. *J. Phys. Conf. Ser.* **2019**, *1294*, 022005. [CrossRef]
21. Lin, C.F.; Kao, C.H.; Lin, C.Y.; Liu, Y.W.; Wang, C.H. The electrical and physical characteristics of Mg-doped ZnO sensing membrane in EIS (electrolyte–insulator–semiconductor) for glucose sensing applications. *Results Phys.* **2020**, *16*, 102976. [CrossRef]
22. Ghirardi, M.L. Implementation of photobiological H_2 production: The O_2 sensitivity of hydrogenases. *Photosynth. Res.* **2015**, *125*, 383–393. [CrossRef] [PubMed]
23. Goodwin, C.A.; Ortu, F.; Reta, D.; Chilton, N.F.; Mills, D.P. Molecular magnetic hysteresis at 60 kelvin in dysprosocenium. *Nature* **2017**, *548*, 439–442. [CrossRef] [PubMed]
24. Sheikh, S.Z.; Wright, J.T.; Siemion, A.; Enriquez, J.E. Choosing a maximum drift rate in a SETI search: Astrophysical considerations. *Astrophys. J.* **2019**, *884*, 14. [CrossRef]
25. Pan, R.; Duque, J.V.F.; Martins, M.F.; Debenest, G. Application of a neural fuzzy model combined with simulated annealing algorithm to predict optimal conditions for polyethylene waste non-isothermal pyrolysis. *Heliyon* **2020**, *6*, e05598. [CrossRef]
26. Stobinski, L.; Lesiak, B.; Malolepszy, A.; Mazurkiewicz, M.; Mierzwa, B.; Zemek, J.; Jiricek, P.; Bieloshapka, I. Graphene oxide and reduced graphene oxide studied by the XRD, TEM and electron spectroscopy methods. *J. Electron Spectrosc. Relat. Phenom.* **2014**, *195*, 145–154. [CrossRef]
27. Li, Y.; Yang, J.; Pan, Z.; Tong, W. Nanoscale pore structure and mechanical property analysis of coal: An insight combining AFM and SEM images. *Fuel* **2020**, *260*, 116352. [CrossRef]
28. Polakof, S.; Panserat, S.; Soengas, J.L.; Moon, T.W. Glucose metabolism in fish: A review. *J. Comp. Physiol. B* **2012**, *182*, 1015–1045. [CrossRef]
29. Summar, M.L.; Koelker, S.; Freedenberg, D.; Le Mons, C.; Haberle, J.; Lee, H.-S.; Kirmse, B.; Registry, T.E.; Members of the Urea Cycle Disorders Consortium. The Incidence of Urea Cycle Disorders. *Mol. Genet. Metab.* **2013**, *110*, 179–180. [CrossRef]